Optical constants and structural properties of thin gold films

Yakubovsky, Dmitry I.; Arsenin, Aleksey V.; Stebunov, Yury V.; Fedyanin, Dmitry Yu; Volkov, Valentyn S.

Published in:
Optics Express

DOI:
10.1364/OE.25.025574

Publication date:
2017

Document version
Publisher's PDF, also known as Version of record

Research Article | Vol. 25, No. 21 | 16 Oct 2017 | OPTICS EXPRESS 25574
Optics EXPRESS

Optical constants and structural properties of thin gold films

DMITRY I. YAKUBOVSKY,[1,4] ALEKSEY V. ARSENIN,[1,2] YURY V. STEBUNOV,[1,2] DMITRY YU. FEDYANIN,[1] AND VALENTYN S. VOLKOV[1,3,5]

[1]*Laboratory of Nanooptics and Plasmonics, Moscow Institute of Physics and Technology, 9 Institutsky Lane, Dolgoprudny, 141700, Russia*
[2]*GrapheneTek, 42-1 Bolshoy Boulevard, Skolkovo Innovation Center, 143026, Russia*
[3]*SDU Nano Optics, Mads Clausen Institute, University of Southern Denmark, Campusvej 55, DK-5230 Odense, Denmark*
[4]*dmitrii.yakubovskii@phystech.edu*
[5]*vsv@mci.sdu.dk*

Abstract: We report a comprehensive experimental study of optical and electrical properties of thin polycrystalline gold films in a wide range of film thicknesses (from 20 to 200 nm). Our experimental results are supported by theoretical calculations based on the measured morphology of the fabricated gold films. We demonstrate that the dielectric function of the metal is determined by its structural morphology. Although the fabrication process can be absolutely the same for different films, the dielectric function can strongly depend on the film thickness. Our studies show that the imaginary part of the dielectric function of gold, which is responsible for optical losses, rapidly increases as the film thickness decreases for thicknesses below 80 nm. At the same time, we do not observe a noticeable dependence of optical constants on the film thickness for thicker samples. These findings establish design rules for thin-film plasmonic and nanophotonic devices.

OCIS codes: (310.6860) Thin films, optical properties; (310.1860) Deposition and fabrication; (160.4670) Optical materials; (160.4760) Optical properties; (250.5403) Plasmonics; (120.2130) Ellipsometry and polarimetry.

References and links

1. S. A. Maier, *Plasmonics: Fundamentals and Applications* (Springer, 2007).
2. V. Bochenkov, J. Baumberg, M. Noginov, F. Benz, H. Aldewachi, S. Schmid, V. Podolskiy, J. Aizpurua, K. Lin, T. Ebbesen, A. A. Kornyshev, J. Hutchison, K. Matczyszyn, S. Kumar, B. de Nijs, F. Rodríguez Fortuño, J. T. Hugall, P. de Roque, N. van Hulst, S. Kotni, O. Martin, F. J. García de Abajo, M. Flatté, A. Mount, M. Moskovits, P. Ginzburg, D. Zueco, A. Zayats, S.-H. Oh, Y. Chen, D. Richards, A. Belardini, and P. Narang, "Applications of plasmonics: general discussion," Faraday Discuss. **178**, 435–466 (2015).
3. B. Špačková, P. Wrobel, M. Bocková, and J. Homola, "Optical biosensors based on plasmonic nanostructures: a review," Proc. IEEE **104**(12), 2380–2408 (2016).
4. Y. Fang and M. Sun, "Nanoplasmonic waveguides: towards applications in integrated nanophotonic circuits," Light Sci. Appl. **4**(6), e294 (2015).
5. S. Gwo and C.-K. Shih, "Semiconductor plasmonic nanolasers: current status and perspectives," Rep. Prog. Phys. **79**(8), 086501 (2016).
6. S. Palomba, S. Zhang, Y. Park, G. Bartal, X. Yin, and X. Zhang, "Optical negative refraction by four-wave mixing in thin metallic nanostructures," Nat. Mater. **11**(1), 34–38 (2011).
7. A. Pors, M. G. Nielsen, and S. I. Bozhevolnyi, "Analog computing using reflective plasmonic metasurfaces," Nano Lett. **15**(1), 791–797 (2015).
8. T. Galfsky, J. Gu, E. E. Narimanov, and V. M. Menon, "Photonic hypercrystals for control of light-matter interactions," Proc. Natl. Acad. Sci. U.S.A. **114**(20), 5125–5129 (2017).
9. A. F. Mayadas and M. Shatzkes, "Electrical-resistivity model for polycrystalline films: the case of arbitrary reflection at external surfaces," Phys. Rev. B **1**(4), 1382–1389 (1970).
10. A. F. Mayadas, M. Shatzkes, and J. F. Janak, "Electrical resistivity model for polycrystalline films: the case of specular reflection at external surfaces," Appl. Phys. Lett. **14**(11), 345–347 (1969).
11. J. Sotelo, J. Ederth, and G. Niklasson, "Optical properties of polycrystalline metallic films," Phys. Rev. B **67**(19), 195106 (2003).
12. K. M. McPeak, S. V. Jayanti, S. J. P. Kress, S. Meyer, S. Iotti, A. Rossinelli, and D. J. Norris, "Plasmonic films can easily be better: rules and recipes," ACS Photonics **2**(3), 326–333 (2015).

#301811 https://doi.org/10.1364/OE.25.025574
Journal © 2017 Received 7 Jul 2017; revised 28 Aug 2017; accepted 5 Sep 2017; published 6 Oct 2017

Optics EXPRESS

13. D. Yu. Fedyanin, D. I. Yakubovsky, R. V. Kirtaev, and V. S. Volkov, "Ultralow-loss CMOS copper plasmonic waveguides," Nano Lett. **16**(1), 362–366 (2016).
14. L. Leandro, R. Malureanu, N. Rozlosnik, and A. Lavrinenko, "Ultrathin, ultrasmooth gold layer on dielectrics without the use of additional metallic adhesion layers," ACS Appl. Mater. Interfaces **7**(10), 5797–5802 (2015).
15. G. V. Naik, V. M. Shalaev, and A. Boltasseva, "Alternative plasmonic materials: beyond gold and silver," Adv. Mater. **25**(24), 3264–3294 (2013).
16. P. Yu. Kuryoz, L. V. Poperenko, and V. G. Kravets, "Correlation between dielectric constants and enhancement of surface plasmon resonances for thin gold films," Phys. Status Solidi., A Appl. Mater. Sci. **210**(11), 2445–2455 (2013).
17. E.-T. Hu, Q.-Y. Cai, R.-J. Zhang, Y.-F. Wei, W.-C. Zhou, S.-Y. Wang, Y.-X. Zheng, W. Wei, and L.-Y. Chen, "Effective method to study the thickness-dependent dielectric functions of nanometal thin film," Opt. Lett. **41**(21), 4907–4910 (2016).
18. M.-Y. Zhang, Z.-Y. Wang, T.-N. Zhang, Y. Zhang, R.-J. Zhang, X. Chen, Y. Sun, Y.-X. Zheng, S.-Y. Wang, and L.-Y. Chen, "Thickness-dependent free-electron relaxation time of Au thin films in near-infrared region," J. Nanophotonics **10**(3), 033009 (2016).
19. H. Reddy, U. Guler, A. V. Kildishev, A. Boltasseva, and V. M. Shalaev, "Temperature-dependent optical properties of gold thin films," Opt. Mater. Express **6**(9), 2776–2802 (2016).
20. H. Qian, Y. Xiao, D. Lepage, L. Chen, and Z. Liu, "Quantum electrostatic model for optical properties of nanoscale gold films," Nanophotonics **4**(1), 413–418 (2015).
21. X. D. Li, T. P. Chen, Y. Liu, and K. C. Leong, "Evolution of the localized surface plasmon resonance and electron confinement effect with the film thickness in ultrathin Au films," J. Nanopart. Res. **17**(2), 67 (2015).
22. M. A. Ordal, L. L. Long, R. J. Bell, S. E. Bell, R. R. Bell, R. W. Alexander, Jr., and C. A. Ward, "Optical properties of the metals Al, Co, Cu, Au, Fe, Pb, Ni, Pd, Pt, Ag, Ti, and W in the infrared and far infrared," Appl. Opt. **22**(7), 1099 (1983).
23. D. Yu. Fedyanin, A. V. Krasavin, A. V. Arsenin, and A. V. Zayats, "Surface plasmon polariton amplification upon electrical injection in highly integrated plasmonic circuits," Nano Lett. **12**(5), 2459–2463 (2012).
24. I. Kojima and B. Li, "Structural characterization of thin films by X-ray reflectivity," Rigaku J. **16**(2), 31–41 (1999).
25. T. C. Huang, R. Giiles, and G. Will, "Thin-film thickness and density determination from X-ray reflectivity data using a conventional power diffractometer," Thin Solid Films **230**(2), 99–101 (1993).
26. J. H. Park, P. Ambwani, M. Manno, N. C. Lindquist, P. Nagpal, S.-H. Oh, C. Leighton, and D. J. Norris, "Single-crystalline silver films for plasmonics," Adv. Mater. **24**(29), 3988–3992 (2012).
27. A. Kossoy, V. Merk, D. Simakov, K. Leosson, S. Kéna-Cohen, and S. A. Maier, "Optical and structural properties of ultra-thin gold films," Adv. Opt. Mater. **3**(1), 71–77 (2015).
28. K.-P. Chen, V. P. Drachev, J. D. Borneman, A. V. Kildishev, and V. M. Shalaev, "Drude relaxation rate in grained gold nanoantennas," Nano Lett. **10**(3), 916–922 (2010).
29. Q. G. Zhang, X. Zhang, B. Y. Cao, M. Fujii, K. Takahashi, and T. Ikuta, "Influence of grain boundary scattering on the electrical properties of platinum nanofilms," Appl. Phys. Lett. **89**(11), 114102 (2006).
30. X. Zhang, X. Song, X.-G. Zhang, and D. Zhang, "Grain boundary resistivities of polycrystalline Au films," EPL **96**(1), 17010 (2011).
31. M. Wei-Gang, W. Hai-Dong, Z. Xing, and T. Koji, "Different effects of grain boundary scattering on charge and heat transport in polycrystalline platinum and gold nanofilms," Chin. Phys. B **18**(5), 2035–2040 (2009).
32. G. Chen, P. Hui, K. Pita, P. Hing, and L. Kong, "Conductivity drop and crystallites redistribution in gold film," Appl. Phys., A Mater. Sci. Process. **80**(3), 659–665 (2005).
33. W. G. Ma, H. D. Wang, X. Zhang, and W. Wang, "Experiment study of the size effects on electron-phonon relaxation and electrical resistivity of polycrystalline thin gold films," J. Appl. Phys. **108**(6), 064308 (2010).
34. P. B. Johnson and R. W. Christy, "Optical constants of the noble metals," Phys. Rev. B **6**(12), 4370–4379 (1972).
35. G. R. Parkins, W. E. Lawrence, and R. W. Christy, "Intraband optical conductivity σ(ω,T) of Cu, Ag, and Au: contribution from electron-electron scattering," Phys. Rev. B **23**(12), 6408–6416 (1981).
36. Y. F. Zhu, X. Y. Lang, W. T. Zheng, and Q. Jiang, "Electron scattering and electrical conductance in polycrystalline metallic films and wires: impact of grain boundary scattering related to melting point," ACS Nano **4**(7), 3781–3788 (2010).
37. E. H. Sondheimer, "The mean free path of electrons in metals," Adv. Phys. **1**(1), 1–42 (1952).
38. E. Kretschmann, "Die Bestimmung optischer Konstanten von Metallen durch Anregung von Oberflachenplasmaschwingugnen," Z. Phys. **241**(4), 313–324 (1971).
39. M. Yamamoto, "Surface plasmon resonance (SPR) theory: tutorial," Rev. Polarogr. **48**(3), 209–237 (2002).
40. Y. V. Stebunov, O. A. Aftenieva, A. V. Arsenin, and V. S. Volkov, "Highly sensitive and selective sensor chips with graphene-oxide linking layer," ACS Appl. Mater. Interfaces **7**(39), 21727–21734 (2015).

1. Introduction

Nanoscale thin metal films are an inherent part of various nanophotonic and plasmonic applications [1,2], such as high-sensitive sensors [3], plasmonic circuits [4], nanolasers [5], optical metamaterials and metasurfaces [6,7], photonic hypercrystals [8], among others.

Optics EXPRESS

Hence, investigation of the optical absorption of metal through interband and intraband electron transitions is an essential input for a comprehensive understanding of the correlation between the metallic films structure and plasmonic/nanophotonic device intrinsic characteristics. Thus, it has been shown that for polycrystalline metal films, the electron scattering at surfaces and grain boundaries contributes strongly to losses [9,10] affecting the complex dielectric function [11]. The exhaustive study of the structural and optical properties of various materials, including traditional plasmonic metals (Au, Ag, Cu, and Al) [12–14] and alternative plasmonic materials (TiN, TCO and others) [15], has been reported with a considerable interest shown in thin films (with the thickness of less than 50 nm) for which a change in the optical properties has been observed as a function of their thickness under constant evaporation regimes [16–18]. Furthermore, the temperature-dependent optical properties of single- and polycrystalline gold thin films were also recently studied [19].

The thickness of the metallic films used for a particular plasmonic application may vary from a few tens to hundreds of nanometers. Therefore, understanding of how the optical properties of metal films depend on thickness is important for improved theoretical studies, numerical modeling and overall optimized performance of plasmonic devices. In this context, it is important to note that a series of rules and recipes to aid researchers in depositing thick metallic films with structural and optical properties optimized for plasmonic applications has already been reported [12]. Here, one should also keep in mind that despite the abundance of materials which are in principle suitable for plasmonic applications (i.e., characterized by a significantly high real part ε' of permittivity and a low imaginary part $\varepsilon'' << |\varepsilon'|$ responsible for losses), gold is still the most commonly used due to its resistance to oxidation, relatively good temperature stability and low loss in the visible and NIR ranges.

The purpose of the present study is therefore to deal with some of the questions remain unanswered regarding the structural and optical properties of *thin* (!) gold films. For this purpose, the high-quality gold films of various thicknesses (ranging from ~20 to 200 nm) were deposited on silicon substrate by use of conventional e-beam evaporation (EBE) technique. Regarding the films thickness range (which we chose to work with), it is important to note that once the film thickness is less than 20 nm one can get island or highly roughened film surfaces and quantum confinement effects need to be considered [20,21]. At the same time, the films with a thickness of more than 200 nm are guaranteed to behave as a bulk metal. Films were characterized by X-ray diffractometry (XRD) and atomic force microscopy (AFM) to study the structural morphology, by the four-point probe to determine the electrical properties and by spectroscopic ellipsometry to determine the optical constants in the spectral range from 300 to 2000 nm. The optical constants measurements were analyzed by the free-electron Drude model and the Mayadas-Shatzkes (MS) theory, which predicts the optical losses and dc electrical conductivity values based on the structural properties of the gold films [10,22,23].

2. Sample fabrication and methods

Thin gold films were deposited on a chemically pre-cleaned silicon Si (100) wafer (the native oxide thickness was measured to be ~1.5 nm) without any adhesion layer. The deposition was performed using gold pellets with a purity of 99.999% (Kurt J. Lesker) and the EBE procedure employing the Nano-Master NEE-4000 system. The base pressure in the vacuum chamber before the evaporation process was as low as $5 \cdot 10^{-7}$ Torr, and it increased to $(5 \pm 1) \cdot 10^{-6}$ Torr during evaporation. The nominal thicknesses of the deposited films 20 – 200 nm and the deposition rate 0.7 – 1 A/s were monitored by the quartz-crystal mass-thickness sensor mounted in the vacuum chamber. The thickness of thin films deposition was independently estimated by step height AFM measurements (by use of a commercial NT-MDT Ntegra microscope) and the root-mean-square (RMS) surface roughness value was determined for each film. The accuracy of film thickness evaluation was additionally verified

Optics EXPRESS

by X-ray reflectometry (XRR) analysis, which is a high precision, non-destructive and fast method to determine the thin layer thickness of different materials [24–27]. The X-ray reflectivity measurements of Au thin films (25, 39 and 53 nm thick) were performed using the Thermo ARL X'TRA X-ray diffractometer and the corresponding reflectivity curves were recorded with a 2θ-scan in the range of 0.6° to 3.3°. The XRR data recorded for each Au film were used to obtain the corresponding film thickness, which was extracted as a fit parameter from the adjustment of the simulation curve to experimental reflection 2θ-scan.

The properties of the polycrystalline structure of Au films as a function of the film thickness were systematically investigated from XRD measurements using conventional scanning methods (with the diffraction signal being collected at grazing incidence in the $\theta/2\theta$ mode). The scan was performed at the angle range of $2\theta = 37 - 39.5°$ and the intensive peak of Bragg reflection with a peak center position at $2\theta_{[111]} = 38.2°$ of Au(111) was identified. Next, the average grain size D was estimated by the Debye-Scherrer Eq. (1), which relates the size of Au crystallites in a thin film to the broadening of the peak in the experimental XRD pattern [28–31]

$$D = \frac{\lambda}{\sqrt{\beta^2 + \beta_{std}^2}\cos\theta} \tag{1}$$

where λ = 0.154 nm is the wavelength of the X-ray radiation, θ – is the diffraction angle, β – is the full-width at half-maximum (FWHM) of the peak, $\beta_{std} = 0.131$ – is the instrumental broadening measured with the corundum single crystal standard (SRM NIST).

The dielectric function spectra of the studied Au thin films were evaluated from data measured using variable angle spectroscopic ellipsometer VASE® by J. A. Woollam Co. (Lincoln, NE) in the photon energy range from 4.13 to 0.62 eV, (i.e., photon wavelengths 300 – 2000 nm). Ψ and Δ ellipsometry parameters were measured at two angles of incidence (70° and 75°) and the corresponding experimental dielectric function values were extracted by the numerical iteration fitting procedure using WVASE® spectroscopic ellipsometry software provided by the manufacturer. Here, we emphasize that the thickness of the Au film was accurately measured independently using the AFM, which enabled us to measure the dielectric function of thin Au films precisely. At the same time, we neglect the influence of the surface roughness on the optical measurements owing to its small values (RMS ≈1.0 nm) [12,26]. Finally, all deposited Au films have been taken for electrical dc-resistive properties measurement by using the Jandel RM3000 four-point probe system.

3. Results and discussion

The surface morphology and thickness of the thin Au films were both investigated by tapping mode AFM. The line scans have been performed for films of different thicknesses over the area with the largest difference between the heights of the step features. Several AFM scans of the same area (and at the same scanning parameters) were performed for each of the samples proving that EBE is a powerful technique for preparing uniform films of controlled thickness. Thus, for example, Fig. 1(a) demonstrates a typical line-scan of the thin Au film surface revealing height-step of about 25 nm which is found to be close to the film thickness determined from the XRR data. The comparison between the results of XRR and AFM thickness measurements for different films is shown in the inset of Fig. 1(b). These values are found to be in good agreement for all tests (within an interval of about 1 nm).

Figure 2 shows typical AFM images (~1.5 × 1.5 μm^2) of 44 and 117 nm-thick Au films evaporated onto silicon substrates at the same low deposition rate. It can be seen that for 44 nm-thick film the estimated lateral average grain size goes to ~41 ± 12 nm [Fig. 2(a)]. For the thicker film of 117 nm [Fig. 2(b)] the same kind of surface morphology is observed; however, the film consists of bigger grains (~57 ± 15 nm) and there are more big hillocks on the

Optics EXPRESS

surface. The RMS surface roughness for thin Au films of different thicknesses is summarized in Table 1 and found to be increasing with the thickness up to (but not exceeding) 1.7 nm for thicker films. The main parameters affecting the uniformity/roughness of the film are deposition rate and temperature of the substrate; however, in current experiment the substrate was kept at an ambient temperature (in the range of 20 C to 30 C) and the deposition rate was as low as 0.7 – 1 A/s, so the results show good, uniform characteristics. However, due to the limited imaging resolution of the AFM, more detailed structural features are not discernible.

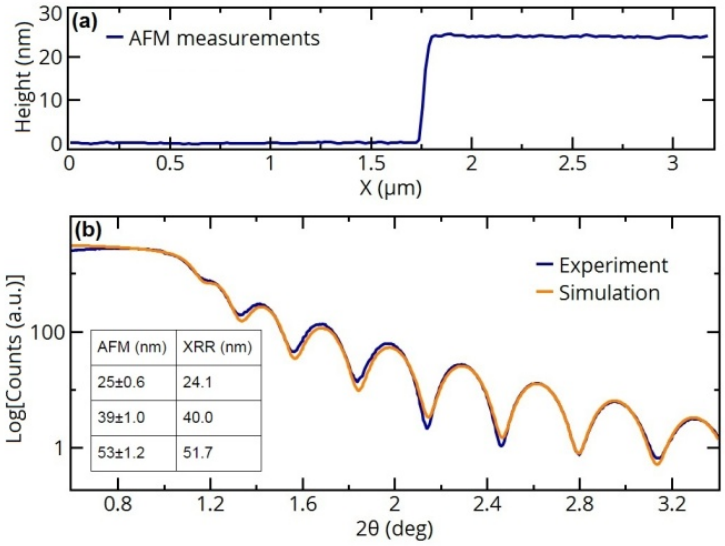

Fig. 1. (a) Surface profile of the step height imaged with AFM, which gives 25 nm for the film thickness, and (b) results of the XRR curve fitting, which yields the film thickness of 24.1 nm. Inset in (b) represents a comparison between the results of XRR and AFM thickness measurements for three different thin films.

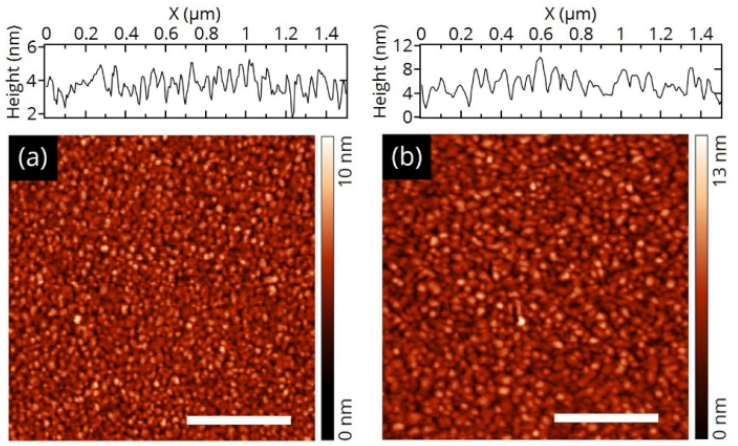

Fig. 2. AFM surface morphology images of the deposited Au films. The film thickness is found to be close to ~44 nm (a) and ~117 nm (b). Scale bar in both panels is 500 nm. AFM scan profiles were used to estimate average grain size (~41 ± 12 and ~57 ± 15 nm) and RMS roughness values (~1.05 and ~1.53 nm) for both films, respectively.

Optics EXPRESS

Table 1. RMS roughness of Au thin films of various thicknesses estimated from the corresponding AFM images

t (nm)	39	44	53	66	78	83	117	176
RMS (nm)	0.72	1.05	1.08	1.12	1.15	1.40	1.53	1.70

To gain further information on the structural properties of the Au thin films, the XRD measurements were performed on these samples (see Fig. 3) showing that the average crystallite size (determined by diffractometry) agrees well with the average grain size estimated from the AFM measurements. Moreover, with increasing film thickness the results of XRD and AFM analysis are showing the improvement of the intrinsic structural homogeneity of the Au films, which is indicated by narrowing of the diffraction peak, as seen in Fig. 3(a). Figure 3(b) demonstrates a monotonically increasing nonlinear dependence of the average crystallite size D with the film thickness, which is found to be in a good qualitative agreement with the findings reported previously for Au polycrystalline films [32,33]. Thus, the grain boundary scattering contribution in optical losses is expected to be lower for thicker films [28].

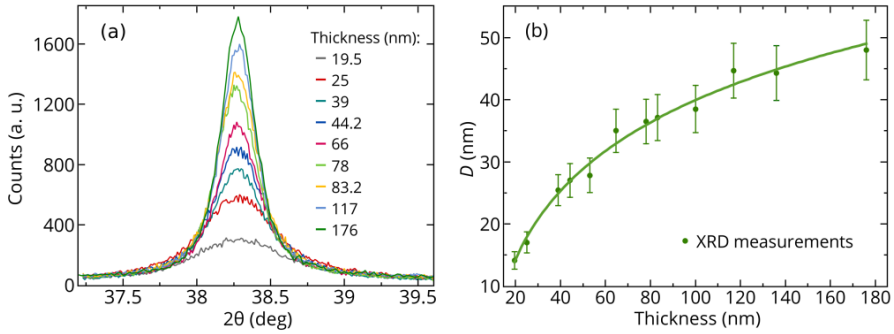

Fig. 3. XRD $\theta/2\theta$ measurements of the deposited gold films. (a) Au (111) diffraction peaks of different colors corresponding to various film thicknesses. (b) The average crystallite size estimated for different films versus films thickness (with a nonlinear curve fitted to experimental data).

To investigate this phenomenon more thoroughly we used spectroscopic ellipsometry measurements so that optical constants, refractive index n and extinction coefficient k could be extracted accurately for all deposited Au films. Figure 4 demonstrates the real $\varepsilon' = n^2 - k^2$ and imaginary $\varepsilon'' = 2nk$ parts of the dielectric function that were measured for each film. For comparison, data from Johnson and Christy [34] are also plotted. Our measurements suggest that the value of ε'' (that govern optical losses in Au films) gets lower for thicker films. In Fig. 4 one can see an imaginary part of the dielectric function ε'' that varies significantly for different film thicknesses (generally, ε'' tends to decrease while the film thickness increases). At the same time, we did not observe a noticeable dependence of ε' on the film thickness.

Optics EXPRESS

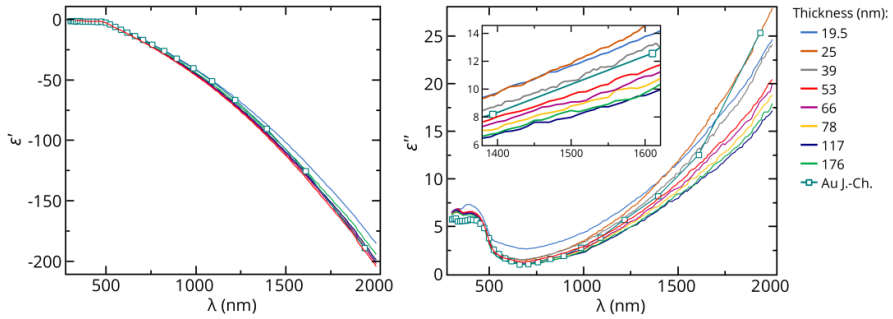

Fig. 4. The measured real ε' and imaginary ε'' parts of the dielectric functions of Au films for several selected thicknesses (also see Table 2 in Appendix). Corresponding values of the film thicknesses (marked by different colors) are listed in the right panel.

To characterize the optical properties of Au thin films of different thickness we performed fitting of the obtained experimental dependencies for ε' and ε'' by the Drude model describing optical response of metals and expressed by:

$$\varepsilon = \varepsilon' + i\varepsilon'' = \varepsilon_\infty - \frac{\omega_p^2}{\omega^2 + i\gamma\omega} = \varepsilon_\infty - \frac{\omega_p^2}{\omega^2 + \gamma^2} + i\frac{\gamma\omega_p^2}{\omega\left(\omega^2 + \gamma^2\right)} \qquad (2)$$

where ε_∞ – is the infinite-frequency dielectric constant, ω_p – is the plasma frequency of metal and γ – is the damping parameter of the Drude model. The imaginary part of the dielectric function $\varepsilon'' = \gamma\omega_p^2 / (\omega(\omega^2 + \gamma^2))$ is responsible for the optical absorption in metal. In order to analyze the influence of film thickness on the optical losses we have implemented a fitting procedure to define parameters ω_p, ε_∞ and the damping rate γ by using the experimental values of ε' and ε'' (Fig. 4). Meanwhile, the variation of the damping term γ with film thickness is represented in Fig. 5 (displayed in yellow squares).

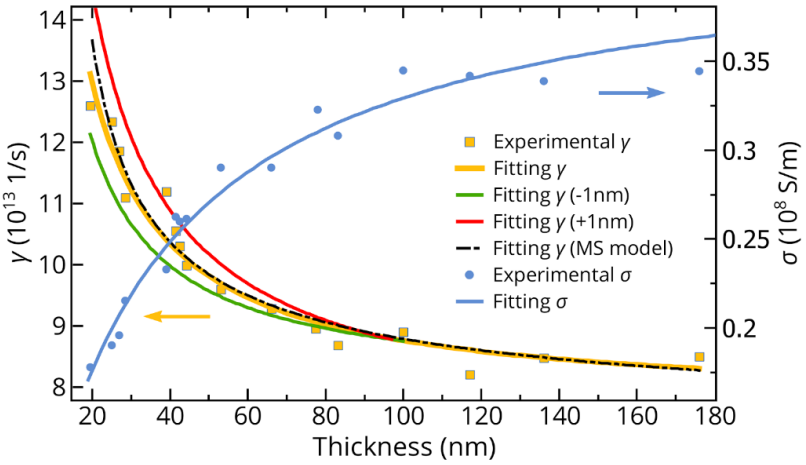

Fig. 5. Experimentally extracted damping rate γ value (yellow squares) as a function of the film thickness. The solid lines (used to guide the eye) represent a nonlinear approximation of experiments by the least-square method. Red and green lines show an approximation of the damping rate values calculated for the film thickness variations of –1 nm (green)/+1 nm (red), respectively. Black dashed line shows the theoretical behavior of the damping rate based on MS model, which fits the data of the experimental dependence. Thickness dependence of conductivity is represented in blue.

Optics EXPRESS

The Drude damping term γ (which defines the total electron relaxation rate) can be represented as $\gamma = \gamma_{ep} + \gamma_{gb} + \gamma_s$, where γ_{ep} – is the electron-phonon scattering, γ_{gb} – is the electron-grain boundary scattering rate and γ_s – is the scattering on the film surface [11,23]. According to these considerations, the structural-dependent scattering contributions γ_{gb} and γ_s become stronger with the decrease of average crystallite size D and film thickness t. Indeed, it was found that while the film thickness increases the Drude damping parameter γ decreases, which leads to the decrease of $\varepsilon"$ (as pointed in the inset of Fig. 4). Figure 5 shows a drastic increase of the damping term in the range of thicknesses between ~20 and 80 nm (along with only marginal changes of γ for films thicker than 80 nm). The latter should be attributed to the stronger contribution of the electron-grain boundaries scattering γ_{gb} for the thinner samples.

To correlate the measured optical properties with the polycrystalline structure of Au films we have compared the results of the extracted damping rate γ with the theoretical model. For that purpose the contribution of the electron-grain boundary scattering γ_{gb} to the total damping rate of Au films was modeled using the Mayadas-Shatzkes (MS) theory, which includes defined values of the mean grain size [10,23] and given by

$$\gamma_{gb} = \gamma_{ep}\left\{\left[1-\frac{3}{2}\alpha+3\alpha^2-3\alpha^3\ln\left(1+\frac{1}{\alpha}\right)\right]^{-1}-1\right\} \quad (3)$$

where $\alpha = \frac{\Lambda}{D}\left(\frac{R}{1-R}\right)$, γ_{ep} – is the electron relaxation rate in bulk Au due to the electron-phonon scattering ($\gamma_{ep} = 4.6\cdot10^{13}$ 1/s at room temperature) [35], R – is the grain-boundary reflection coefficient (~0.2 - 0.8 for Au [30,36]), $\Lambda = 39$ nm [37] – is the mean free path for electron conduction in bulk Au. In this model we assume the average crystallite size $D(t)$ to be a function of thickness taken from the nonlinear approximation curve of the XRD measured crystallite size dependence (green solid curve in Fig. 3(b)). The comparison of experimentally measured and calculated (using Eq. (3)) Drude damping rates demonstrates a good agreement, as indicated by the merging of solid yellow and black dashed lines in Fig. 5. We also found the crystallite boundary reflection coefficient $R = 0.31$ and the residual damping term $\gamma_s = 1.35\cdot10^{13}$ 1/s attributed to the scattering on a rough surface, which provides the best fit of the model to data. It should be noted that the grain boundary reflection coefficient obtained from our analysis is close to the values reported previously [36]. Since our XRD measurements showed the increase of D with thickness (see Fig. 3), the contribution of the electron scattering on crystallite boundaries γ_{gb} becomes weaker. According to the MS theory, this is due to the fact that the scattering has stronger influence when crystallites become smaller or compared with the mean-free-path of electrons in Au (~40 nm).

In order to understand how the accuracy of the film thickness measurements affects the optical properties, we have theoretically studied the influence of uncertainty in the determined film thickness on the resulting damping factor γ. For this purpose three-media ellipsometry model [12,26] has been used to extract the real and imaginary parts of the dielectric function for the films with the thicknesses being 1 nm larger/smaller than those to be measured experimentally. The calculated values of the damping rate for the film thickness variations of ± 1 nm were plotted together with the experimental dependence of the damping rate on thickness (displayed in yellow squares) in Fig. 5. As it can be seen, the most noticeable

Optics EXPRESS

deviation in the value of γ (due to ± 1 nm thickness variation) was observed for film thicknesses below 80 nm. This clearly demonstrates that the usage of smaller Au thicknesses included in the ellipsometry model leads to an underestimation of measured ε'' and γ of the thin metal film (affecting critically the determination of the optical losses, especially for thinner films).

Optical constants are linked with the dc electrical conductivity σ of polycrystalline metallic films (e.g., it is crucially influenced by the electron scattering at grain boundaries and intrinsic defects). In order to investigate how the thickness-dependent morphology of the film affects ohmic losses, we have used the four-point probe technique to measure the conductivity of Au films. Our results demonstrate the increasing trend of σ with film thickness (see blue dots in Fig. 5), exactly what was expected.

As noted above, polycrystallinity of metallic films influences the performance of different plasmonic devices. To demonstrate this, we investigated the excitation of the surface plasmon resonance (SPR) in gold films characterized by different crystallites sizes D. The SPR excitation was considered according to the Kretschmann's configuration [38], which composes 1) the glass prism with refractive index (RI) 1.523; 2) 47-nm-thick gold films; and 3) the top aqueous layer with RI of 1.33. Dielectric permittivity of gold films was described according to the Eq. (2), where the plasma frequency ω_p and the dependence of the damping term γ on the crystallite size D were previously obtained from ellipsometric and XRD measurements. Using transfer matrix model [39,40], we obtained SPR angular curves for different wavelengths of exciting laser radiation (880, 980, 1310, and 1550 nm) and different crystallites sizes ranging from 14 to 49 nm [Fig. 6(a)]. The main parameters characterizing SPR biosensing include the full-width at half-maximum (FWHM) α_{FWHM} of SPR angular curve and the sensitivity to RI changes S_{RI} which equals the ratio of the shift of SPR angle $\Delta\alpha$ to the corresponding change of RI of the media Δn above the metal film [3]:

$$S_{RI} = \frac{\Delta\alpha}{\Delta n}$$

Both S_{RI} and FWHM values depend on a dielectric constant of Au films, where the first parameter is characterized mostly by the real part of dielectric function ε'. However, the second parameter is determined by both ε' and ε'', which explains FWHM broadening for higher crystallite sizes and lower operating wavelengths. The detection limit of the SPR biosensor based on Kretschmann's configuration is proportional to the figure of merit (FOM), which is the ratio of the sensitivity to RI changes S_{RI} to the full-width at half-maximum α_{FWHM}. The α_{FWHM} (solid lines) and FOM (dashed lines) corresponding to the above-stated wavelengths and crystallites sizes are shown in Fig. 6(b), which demonstrates the increase of FOM up to 60% for different crystallites sizes.

Optics EXPRESS

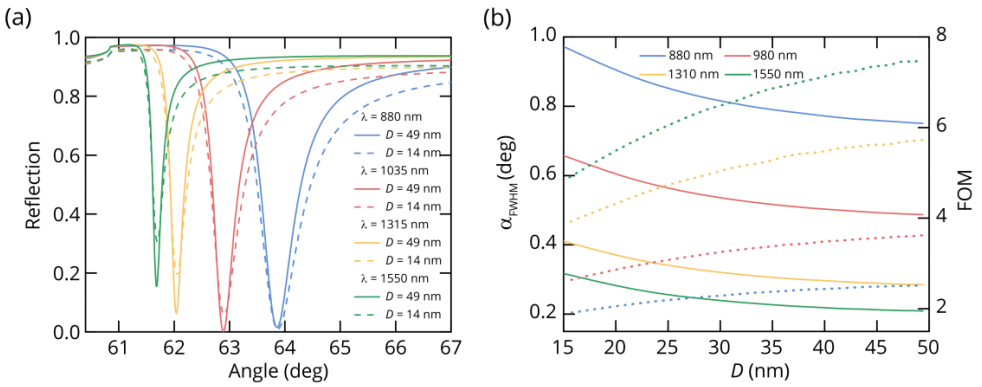

Fig. 6. (a) SPR angular reflectivity curves for gold films with different crystallinity and at four different wavelengths of laser radiation. (b) Full-width at half-maximum and figure of merit for SPR biosensing based on thin gold films with different crystallinity.

4. Conclusion

To summarize, thin films of polycrystalline gold of different thicknesses were grown by conventional e-beam evaporation technique on silicon substrates at room temperature. The effect of the thickness variation on the structural and optical properties of these films was investigated in great detail by using various characterization techniques. The proposed method utilizes an accurate estimation of the films thickness and the analysis of their morphology (by use of AFM, XRR, and XRD) to enable the determination and reproducibility of the optical constants data (by use of ellipsometry measurements in visible and NIR ranges). With this approach, we were able to demonstrate the reliable correlation between the dielectric function of the thin gold film and its thickness-dependent structural morphology. The salient conclusions arising from this detailed study are recapitulated below:

- The results of XRD and AFM analysis show that the grain sizes of the Au thin films increase with increasing film thickness from ~20 to 176 nm (i.e., the intrinsic structural homogeneity of gold improves for thicker films).
- The spectroscopic ellipsometry and four-point probe measurements were conducted to determine the optical constants and the electrical properties of the fabricated Au films. Here, special attention was paid to films thickness measurements (by use of XRR and AFM) which are critical for the accuracy of the optical constants estimation.
- We reported the real and imaginary parts of the dielectric function for the visible and NIR ranges and demonstrated that the optical losses increase significantly with the reduction of the film thickness lower than ~80 nm.
- It is found that while the film thickness increases the Drude damping parameter γ demonstrates a drastic increase in the range of thicknesses between ~20 and 80 nm, which should be attributed to the larger contribution of the electron-grain boundaries scattering at smaller thicknesses (that increases overall optical losses).
- The conductivity of the film was found to increase with increasing film thickness (which is inversely related to the dependence obtained for Drude damping factor γ), demonstrating the influence of a change in the polycrystalline structure of gold films on their optical and electrical properties.

Optics EXPRESS

- The experimental results are confirmed by theoretical investigations based on the measured morphology of the fabricated gold films.
- Finally, issues of the appliance of thin Au films for practical plasmonic devices are discussed in the context of the films crystallinity influence on the performance characteristics of the SPR biosensor. In particular, it is shown that the increase of average crystallite size from 14 to 49 nm results in the increase of SPR biosensor figure of merit up to 60%.

Appendix

In this Appendix, we present tabular data for the dielectric permittivity of thin gold films with the following thicknesses: 25, 53, and 117 nm.

Table 2. The measured real ε' and imaginary ε'' parts of thin gold films

λ, nm	25 nm		53 nm		117 nm	
	ε'	ε''	ε'	ε''	ε'	ε''
300	–1.09	6.23	–1.08	6.67	–1.13	6.42
310	–0.99	6.39	–0.97	6.82	–1.01	6.56
320	–0.88	6.47	–0.81	6.90	–0.86	6.68
330	–0.79	6.47	–0.66	6.89	–0.70	6.70
340	–0.76	6.39	–0.56	6.77	–0.59	6.60
350	–0.85	6.29	–0.63	6.57	–0.61	6.40
360	–1.04	6.28	–0.85	6.46	–0.82	6.29
370	–1.20	6.31	–1.08	6.49	–1.03	6.30
380	–1.31	6.35	–1.22	6.54	–1.14	6.34
390	–1.39	6.39	–1.31	6.59	–1.22	6.36
400	–1.44	6.40	–1.36	6.59	–1.27	6.37
410	–1.49	6.35	–1.40	6.56	–1.31	6.33
420	–1.55	6.29	–1.44	6.48	–1.34	6.24
430	–1.60	6.17	–1.48	6.36	–1.37	6.12
440	–1.65	6.01	–1.52	6.19	–1.39	5.95
450	–1.71	5.79	–1.55	5.95	–1.42	5.69
460	–1.79	5.49	–1.60	5.61	–1.46	5.36
470	–1.92	5.10	–1.69	5.19	–1.54	4.94
480	–2.14	4.61	–1.88	4.63	–1.72	4.37
490	–2.51	4.07	–2.24	3.98	–2.07	3.73
500	–3.03	3.56	–2.82	3.37	–2.63	3.12
510	–3.68	3.14	–3.56	2.88	–3.34	2.65
520	–4.43	2.81	–4.41	2.51	–4.16	2.29
530	–5.14	2.59	–5.18	2.28	–4.91	2.05
540	–5.83	2.40	–5.95	2.10	–5.65	1.87
550	–6.53	2.25	–6.69	1.97	–6.38	1.72
560	–7.23	2.12	–7.43	1.86	–7.10	1.60
570	–7.92	2.02	–8.17	1.77	–7.82	1.50
580	–8.62	1.92	–8.90	1.68	–8.54	1.42
590	–9.33	1.83	–9.63	1.61	–9.24	1.36
600	–10.06	1.77	–10.40	1.56	–9.99	1.29
610	–10.79	1.71	–11.14	1.50	–10.71	1.24
620	–11.51	1.64	–11.90	1.46	–11.44	1.19

Optics EXPRESS

λ, nm	25 nm		53 nm		117 nm	
	ε'	ε''	ε'	ε''	ε'	ε''
630	−12.25	1.59	−12.64	1.40	−12.18	1.14
640	−13.02	1.56	−13.43	1.37	−12.94	1.10
650	−13.79	1.52	−14.20	1.34	−13.69	1.06
660	−14.56	1.50	−14.99	1.31	−14.44	1.03
670	−15.35	1.48	−15.80	1.29	−15.22	1.00
680	−16.15	1.49	−16.63	1.28	−16.03	0.99
690	−16.95	1.47	−17.44	1.29	−16.82	0.99
700	−17.76	1.49	−18.27	1.30	−17.63	1.00
710	−18.56	1.52	−19.10	1.33	−18.42	1.02
720	−19.37	1.55	−19.92	1.36	−19.22	1.04
730	−20.21	1.59	−20.77	1.39	−20.05	1.07
740	−21.03	1.63	−21.61	1.43	−20.86	1.10
750	−21.90	1.68	−22.50	1.46	−21.71	1.12
760	−22.74	1.73	−23.35	1.50	−22.55	1.15
770	−23.56	1.77	−24.17	1.55	−23.35	1.18
780	−24.44	1.83	−25.06	1.60	−24.22	1.22
790	−25.30	1.87	−25.95	1.65	−25.07	1.25
800	−26.16	1.91	−26.82	1.69	−25.93	1.29
810	−27.04	1.97	−27.73	1.74	−26.80	1.33
820	−28.03	2.07	−28.73	1.81	−27.78	1.38
830	−28.79	2.08	−29.46	1.83	−28.49	1.41
840	−29.73	2.16	−30.44	1.89	−29.44	1.45
850	−30.59	2.21	−31.34	1.94	−30.30	1.50
860	−31.62	2.31	−32.40	2.01	−31.34	1.55
870	−32.61	2.41	−33.34	2.06	−32.26	1.59
880	−33.54	2.48	−34.29	2.11	−33.16	1.63
890	−34.35	2.49	−35.19	2.18	−34.02	1.68
900	−35.29	2.57	−36.16	2.23	−34.97	1.74
910	−36.24	2.64	−37.15	2.29	−35.93	1.78
920	−37.24	2.74	−38.13	2.36	−36.87	1.85
930	−38.29	2.85	−39.17	2.43	−37.89	1.90
940	−39.25	2.92	−40.17	2.50	−38.88	1.96
950	−40.26	3.01	−41.21	2.58	−39.90	2.02
960	−41.25	3.09	−42.24	2.64	−40.88	2.07
970	−42.34	3.21	−43.32	2.70	−41.93	2.14
980	−43.35	3.30	−44.38	2.78	−42.96	2.19
990	−44.44	3.42	−45.47	2.84	−44.02	2.23
1000	−45.33	3.46	−46.48	2.89	−44.99	2.27
1010	−46.47	3.60	−47.63	2.94	−46.07	2.31
1020	−47.38	3.65	−48.64	2.95	−47.02	2.33
1030	−48.90	3.90	−49.56	3.30	−48.15	2.69
1040	−50.01	4.02	−50.69	3.39	−49.19	2.76
1050	−51.17	4.13	−51.84	3.48	−50.33	2.87
1060	−52.17	4.20	−52.80	3.58	−51.30	2.93
1070	−53.42	4.36	−54.09	3.68	−52.52	3.03
1080	−54.63	4.52	−55.25	3.81	−53.72	3.10
1090	−55.58	4.54	−56.28	3.87	−54.65	3.18
1100	−56.87	4.69	−57.52	4.00	−55.87	3.29
1110	−58.11	4.89	−58.74	4.07	−57.07	3.37
1120	−59.13	4.98	−59.81	4.17	−58.09	3.50
1130	−60.36	5.15	−61.09	4.32	−59.37	3.60
1140	−61.63	5.27	−62.31	4.43	−60.53	3.73
1150	−62.82	5.37	−63.49	4.55	−61.79	3.78
1160	−64.04	5.51	−64.77	4.67	−63.07	3.88
1170	−65.43	5.73	−66.10	4.82	−64.26	4.00
1180	−66.49	5.79	−67.17	4.93	−65.31	4.11
1190	−67.74	5.94	−68.38	5.02	−66.51	4.24
1200	−69.02	6.11	−69.63	5.18	−67.74	4.34
1210	−70.34	6.19	−71.01	5.31	−69.09	4.51

Optics EXPRESS

λ, nm	25 nm		53 nm		117 nm	
	ε'	ε''	ε'	ε''	ε'	ε''
1220	−71.57	6.43	−72.35	5.46	−70.35	4.58
1230	−72.85	6.59	−73.64	5.57	−71.59	4.69
1240	−74.18	6.75	−74.88	5.74	−72.83	4.85
1250	−75.49	6.92	−76.27	5.81	−74.23	4.94
1260	−76.97	7.13	−77.84	5.94	−75.74	4.98
1270	−78.08	7.16	−78.80	6.08	−76.71	5.12
1280	−79.36	7.32	−80.31	6.22	−77.97	5.14
1290	−80.79	7.53	−81.65	6.36	−79.44	5.30
1300	−82.20	7.75	−83.05	6.49	−80.82	5.53
1310	−83.55	7.93	−84.37	6.58	−82.16	5.60
1320	−84.93	8.10	−85.84	6.76	−83.57	5.63
1330	−86.29	8.27	−87.22	6.94	−84.81	5.81
1340	−87.74	8.51	−88.67	7.09	−86.24	6.01
1350	−89.11	8.73	−89.99	7.21	−87.64	6.09
1360	−90.55	8.94	−91.56	7.40	−89.20	6.28
1370	−91.93	9.12	−93.00	7.45	−90.49	6.33
1380	−93.33	9.31	−94.35	7.63	−91.85	6.49
1390	−94.77	9.53	−95.89	7.81	−93.24	6.57
1400	−96.32	9.68	−97.41	8.02	−94.80	6.79
1410	−97.78	9.98	−99.01	8.19	−96.34	6.93
1420	−99.22	10.19	−100.42	8.30	−97.63	7.00
1430	−100.55	10.25	−101.82	8.41	−99.03	7.10
1440	−102.07	10.52	−103.33	8.56	−100.67	7.33
1450	−103.56	10.74	−104.84	8.71	−102.14	7.63
1460	−105.16	10.94	−106.53	8.91	−103.67	7.61
1470	−106.78	11.27	−108.18	9.12	−105.39	7.62
1480	−108.06	11.40	−109.56	9.23	−106.54	7.81
1490	−109.52	11.64	−111.05	9.37	−108.14	7.90
1500	−111.27	11.81	−112.63	9.60	−109.65	7.96
1510	−112.67	12.15	−114.27	9.77	−111.13	8.19
1520	−114.39	12.40	−115.80	9.81	−112.54	8.37
1530	−115.76	12.60	−117.38	10.01	−114.47	8.51
1540	−117.63	12.90	−119.29	10.23	−116.28	8.73
1550	−118.95	13.01	−120.71	10.34	−117.44	8.71
1560	−120.65	13.30	−122.40	10.69	−119.20	8.89
1570	−122.29	13.49	−124.16	10.92	−120.66	9.04
1580	−123.96	13.79	−125.80	11.04	−122.21	9.28
1590	−125.51	14.13	−127.31	11.05	−123.74	9.48
1600	−127.22	14.53	−128.98	11.31	−125.66	9.52
1610	−128.82	14.70	−130.70	11.54	−127.48	9.72
1620	−130.69	14.98	−132.51	11.73	−129.09	9.93
1630	−132.43	15.22	−134.28	11.77	−130.76	10.11
1640	−134.15	15.54	−136.02	12.13	−132.44	10.14
1650	−135.78	15.79	−137.98	12.20	−134.23	10.38
1660	−137.33	16.21	−139.57	12.53	−135.82	10.54
1670	−139.21	16.52	−141.36	12.65	−137.65	10.67
1680	−140.75	16.71	−142.84	12.88	−139.18	10.71
1690	−142.29	16.85	−144.75	13.13	−140.97	10.86
1700	−143.98	17.49	−146.63	13.32	−142.75	10.98
1710	−145.79	17.55	−148.15	13.53	−144.23	11.09
1720	−147.74	17.90	−150.05	13.80	−146.01	11.35
1730	−149.36	18.18	−151.71	13.85	−147.62	11.56
1740	−150.96	18.43	−153.47	13.97	−149.41	11.66
1750	−152.67	18.65	−155.32	14.14	−150.95	11.94
1760	−154.56	18.95	−157.05	14.39	−152.73	12.14
1770	−156.36	19.29	−158.87	14.64	−154.50	12.26
1780	−158.18	19.60	−160.85	14.91	−156.14	12.54
1790	−159.97	19.94	−162.24	15.06	−157.79	12.68
1800	−161.75	20.27	−164.03	15.28	−159.65	12.78

Optics EXPRESS

λ, nm	25 nm		53 nm		117 nm	
	ε'	ε''	ε'	ε''	ε'	ε''
1810	−163.70	20.75	−165.90	15.36	−161.42	12.98
1820	−165.48	21.00	−167.83	15.67	−163.18	13.13
1830	−167.12	21.26	−169.50	15.97	−164.83	13.28
1840	−168.92	21.58	−171.23	16.22	−166.56	13.31
1850	−170.72	21.95	−173.12	16.37	−168.48	13.67
1860	−172.36	22.21	−174.68	16.66	−170.12	13.84
1870	−174.33	22.56	−176.64	16.82	−172.12	14.05
1880	−176.32	22.99	−178.80	17.04	−173.84	14.18
1890	−177.94	23.27	−180.48	17.23	−175.39	14.33
1900	−180.56	23.93	−184.02	17.71	−178.73	14.84
1910	−182.55	24.40	−185.94	17.87	−180.53	14.90
1920	−184.43	24.83	−188.03	18.02	−182.33	15.18
1930	−186.46	25.13	−189.77	18.43	−184.33	15.48
1940	−188.54	25.50	−191.63	18.61	−186.33	15.78
1950	−190.51	25.90	−193.71	18.86	−188.16	16.17
1960	−192.49	26.20	−195.63	19.22	−190.30	16.21
1970	−194.57	26.57	−197.56	19.57	−192.67	16.52
1980	−196.43	26.99	−199.55	19.98	−194.75	16.63
1990	−198.58	27.48	−201.53	20.15	−196.89	16.85
2000	−200.59	27.89	−203.92	20.41	−198.55	17.14

Funding

Russian Foundation for Basic Research (RFBR) (grants 16-07-00837-a, 16-29-03432-ofi_m); Ministry of Education and Science of the Russian Federation (8.9898.2017/6.7, 16.7162.2017/8.9, RFMEFI59417X0014).